

A novel Sm doped Cr₂O₃ sesquioxide-decorated MWCNTs heterostructured Fenton-like with sonophotocatalytic activities under visible light irradiation

Eshaq Ghada, Amer Mohamed, Ali Khan Moonis, Alothman Zeid A., Sillanpää Mika

This is a Post-print version of a publication
published by Elsevier
in Journal of Hazardous Materials

DOI: 10.1016/j.jhazmat.2021.127812

Copyright of the original publication:

© 2021 Elsevier B.V.

Please cite the publication as follows:

Eshaq, G., Amer, M., Ali, K.M., Alothman, Z.A., Sillanpää, M. (2021). A novel Sm doped Cr₂O₃ sesquioxide-decorated MWCNTs heterostructured Fenton-like with sonophotocatalytic activities under visible light irradiation. Journal of Hazardous Materials. DOI: 10.1016/j.jhazmat.2021.127812

**This is a parallel published version of an original publication.
This version can differ from the original published article.**

1 **A novel Sm doped Cr₂O₃ sesquioxide-decorated MWCNTs heterostructured**
2 **Fenton-like with sonophotocatalytic activities under visible light irradiation**

3 **Gh. Eshaq^{a,b*}, Amer M^c, Moonis Ali Khan^d, Zeid A Alothman^d, Mika Sillanpää^{d,e,f,g}**

4 *^aDepartment of Separation Science, School of Engineering Science, Lappeenranta University of Technology,*
5 *Sammonkatu 12, FI-50130, Mikkeli, Finland*

6 *^bPetrochemicals department, Egyptian Petroleum Research Institute, Nasr City, Cairo 11727, Egypt*

7 *^cDivision of Cardiac Surgery, Heart Centre Siegburg-Wuppertal, University Witten-Herdecke, Germany*

8 *^dChemistry Department, College of Science, King Saud University, Riyadh 11451, Saudi Arabia*

9 *^eFaculty of Science and Technology, School of Applied Physics, University Kebangsaan Malaysia, 43600, Bangi,*
10 *Selangor, Malaysia*

11 *^fSchool of Chemistry, Shoolini University, Solan, Himachal Pradesh, 173229, India*

12 *^gDepartment of Biological and Chemical Engineering, Aarhus University, Nørrebrogade 44, 8000 Aarhus C,*
13 *Denmark*

14
15
16
17
18 **Abstract**

19 Novel Sm doped Cr₂O₃ decorated MWCNTs nanocomposite photocatalyst was successfully
20 prepared by a facile hydrothermal method for metoprolol (MET) degradation. A heterogeneous
21 photo-Fenton like system was formed with the addition of H₂O₂ for ultrasonic irradiation (US),
22 visible light irradiation (Vis) and dual irradiation (US/Vis) systems. The intrinsic characteristics
23 of Sm doped Cr₂O₃ decorated MWCNTs nanocomposite was comprehensively performed using
24 state-of-art characterization tools. Optical studies confirmed that Sm doping shifted the
25 absorbance of Cr₂O₃ towards the visible-light region, further enhanced by MWCNTs
26 incorporation. In this study, degradation of metoprolol (MET) was investigated in the presence
27 of Cr₂O₃ nanoparticles, Sm doped Cr₂O₃ and Sm doped Cr₂O₃ decorated MWCNTs
28 nanocomposites using sonocatalysis and photocatalysis and simultaneously. Several different
29 experimental parameters, including irradiation time, H₂O₂ concentration, catalyst amount, initial
30 concentration, and pH value, were optimized. The remarkably enhanced sonophotocatalytic

31 activity of Sm doped Cr₂O₃ decorated MWCNTs could be attributed to the more formation of
32 reactive radicals and the excellent electronical property of Sm doping and MWCNTs. The rate
33 constant of degradation using sonophotocatalytic system was even higher than the sum of rates
34 of individual systems due to its synergistic performance based on the kinetic data. A plausible
35 mechanism for the degradation of MET over Sm-Cr₂O₃/MWCNTs is also demonstrated by using
36 active species scavenger studies and EPR spectroscopy. Our findings imply that ([•]OH), (h⁺) and
37 ([•]O₂⁻) were the reactive species responsible for the degradation of MET based on the special
38 three-way Fenton-like mechanism and the dissociation of H₂O₂. The durability and stability of
39 the nanocomposite were also performed, and the obtained results revealed that the catalysts can
40 endure the harsh sonophotocatalytic conditions even after fifth cycles. Mineralization
41 experiments using the optimized parameters were evaluated as well. The kinetics and the
42 reaction mechanism with the possible reasons for the synergistic effect were presented.
43 Identification of degraded intermediates also investigated.

44 **Keywords:** Heterogeneous photocatalyst; Synergistic effect; Sm doped; Rare earth; β-blockers.

45 **1. Introduction**

46 Early in 1980s the presence of active pharmaceutical ingredients (APIs) was reported in the
47 aquatic environments (Richardson et al., 1985). Currently, a large number of different APIs with
48 varied concentrations have been detected in the aqueous environment, and even in drinking water
49 resources (Verlicchi et al., 2012; Martínez et al., 2011). Generally, these APIs are discharged
50 from pharmaceutical industries, hospitals, and domestic waters via improperly disposed
51 pharmaceuticals or by human excretions. These APIs are partially metabolized by the body and
52 secreted (Santos et al., 2011) and could be hazardous to human health and aquatic life (Simazaki
53 et al., 2015). Thus, contamination of water with prescribed drugs traces and their metabolites is

54 of great concern. In addition, these recalcitrant organic pollutants turn in municipal sewage
55 system and ultimately enter wastewater treatment plants (WWTP) (Isidori et al., 2009). The
56 conventional treatment plants are ineffective in removing these hazardous compounds.
57 Eventually, they will arrive in aqueous environment and water resources posing potential health
58 threats to living organisms (Chakraborty et al., 2017). Recently, the occurrence of β -blockers has
59 been repeatedly reported in the effluents of many (WWTP) around the world (Marothu et al.,
60 2019). The database of APIs in the Environment of the German Federal Environment Agency
61 records over 1750 entries about the presence of metoprolol in different water bodies worldwide
62 in the year 2018. Also, the highest metoprolol concentrations in surface water and in (WWTP)
63 were detected, amounting to several micrograms per liter in Asia and in Western Europe
64 respectively (Eike, D 2019). Among the most important class of pharmaceutical compounds and
65 from the top prescribed medications worldwide, β -blocker drugs is frequently detected in the
66 environment, and also known as beta-adrenergic blocking agents. Due to blocking the action of
67 epinephrine and norepinephrine on the β -adrenergic receptors of the sympathetic nervous system
68 of the human body, primarily in the heart (Verlicchi et al., 2012; Isidori et al., 2009; Yang et al.,
69 2010). They are used to treat a variety of cardiovascular diseases, like, coronary artery disease,
70 chronic heart failure, arrhythmias, and hypertension (Abramovi' et al., 2011). There per capita
71 use in countries such as United Kingdom, Switzerland, and Finland, has increased to 3.2, 1.1 and
72 0.1 g per year, respectively (Alder et al., 2010). As β -blockers are extensively used in households
73 and hospitals, several measurements have been constantly carried out in hospital wastewater
74 (HWW), surface water and (WWTP) (Gabet-Giraud et al., 2010). Moreover, β -blockers are
75 considered as pseudo-persistent compounds with inconspicuous adverse effects even at low
76 concentration appearing from long-term exposure (Xu et al., 2011). The most commonly

77 prescribed β -blockers medications are, metoprolol (MET), propranolol (PRO) and atenolol
78 (ATE) (Wilde et al., 2014). In recent years, MET is represented by the excessive use, with usage
79 increased by a factor of 4 and as a result, its appearance is expected to increase in aqueous
80 effluents as well (Alder et al., 2010). In Finland, MET is consumed in higher amount per person
81 compared to other European countries. Furthermore, it has been reported that the presence of
82 eight pharmaceutical compounds including β -blockers in twelve Finnish sewage treatment plants
83 (STPs) effluents up to $\mu\text{g/L}$ concentrations of the raw and STPs effluents. Also, in the rivers
84 receiving STPs effluents and MET was the prevailing compound in the effluent samples (Vieno
85 et al., 2007). It should be pointed out that MET has slow in direct hydrolysis and/or photo
86 transformation (Piram et al., 2008). In this context, the most powerful techniques for the
87 treatment of wastewater effluents are advanced oxidation processes (AOPs) and should include
88 in all wastewater treatment plant. AOPs are capable to achieve high destruction with complete
89 decomposition of persistent organic contaminants into CO_2 , H_2O , and inorganic salts. Based on
90 the generation of hydroxyl radicals ($\cdot\text{OH}$), which are highly reactive species that mitigate the
91 deterioration of environment (Molinari et al., 2006; Song et al., 2008). Photocatalytic treatment
92 is proved to be an effective for the degradation of MET and PRO (Romero et al., 2011). An
93 overview on the degradation of β -blockers in the aquatic environment with different
94 photocatalytic procedures found in the literature has been reported by Marothu et al 2019. More
95 recently, the application of graphite-PVC composite as anode (Mussa 2020) and through bio-
96 electro-Fenton (BEF) (Yang et al., 2021) was investigated for the electrochemical degradation of
97 (MET). Moreover, photocatalytic degradation of (MET) using a TiO_2 /natural zeolite composite,
98 UV/chlorine, UV/ H_2O_2 and using AOPs— Quantitative Structure Activity Relationship (QSAR)
99 analysis to predict Eco-toxicity has been studied (Jessica 2021; Gao et al., 2020; Melanie et al.,

2021). The metoprolol removal is about ten times faster with the photo Fenton like process than with the photocatalytic or photolytic processes (Avilés-García et al., 2021). Moreover, the integration between the different AOPs has been found to be promising and highly efficient process. Furthermore, it increases the generation of $\cdot\text{OH}$, within a short time span, speeding up the oxidation process and consequently rising mineralization degree of organic pollutants (Madhavan et al., 2010). Moreover, several recent studies have addressed the possibility of simultaneously using sonolysis (US) and photocatalysis called as sonophotocatalysis (US/UV). This represents an attractive strategy for eco-friendly remediation. Also, it can significantly accelerate the degradation performance and achieve a complete mineralization of recalcitrant organic pollutants synergistically. This combination process increase the generation of $\cdot\text{OH}$ and eliminate the drawbacks associated with the un-combines process (Eshaq et al., 2020). Transition metal ions (Fe(II), Fe(III), Cu (II)) induced decomposition of H_2O_2 and generates different types of reactive oxygen species (ROS) including highly efficient $\cdot\text{OH}$ and $\cdot\text{O}_2^-$ through a redox cycle. These transition metals have been extensively used in classical Fenton and Fenton-like reactions for efficient removal of recalcitrant organic pollutants via oxidation reactions (Collins and TAML, 2002; Shah et al., 2003). As Fe, Cu, and Cr presences in multiple oxidation states from -2 to +6, but only Cr(III) and Cr(VI) species are usually detected in water. Cr(III) and Cr(VI) have been reacted with H_2O_2 to generate $\cdot\text{OH}$ constantly based on Cr(III)/Cr(VI) redox cycle through Fenton-like reactions (Bokare et al., 2014; Pettine et al., 2002). However, Cr(VI), is a human carcinogen Group 'A' with the high potential risks for human health and environmental, causes allergic dermatitis, and pulmonary congestion mutagenic liver damage (Codd et al., 2001). Thus, any addition of Cr (VI) into wastewaters as a reagent is not reasonable, due to its carcinogenicity and higher toxicity. On the other hand, Cr(III) is essential micronutrient for both

123 plants and animals necessary in sugar metabolism (Levina et al., 2005). Furthermore, Cr(III) at
124 pH>5 is precipitated as insoluble chromium hydroxide, while Cr(VI) is completely soluble in
125 water at the same pH. This contrasting toxicity profile for both Cr species is essentially
126 depending on the solubility behaviour of both Cr species (Bokare et al., 2014). Cr is a transition
127 metal-oxide material with potential applicability in optical and electronic devices. Sesquioxide
128 (Cr₂O₃) or Cr(III) is one of the most important p-type semiconductor (Anjum et al., 2018),
129 having a wide band gap of ($E_g \approx 3.4$ eV) (Rajesh kumar et al., 2019), heterogeneous catalysts
130 (He et al., 2002), gas sensor (Stănoiu et al., 2012), and solar energy collector (Teixeira et al.,
131 2001). Cr(III) is kinetically inert and it has the most thermodynamically stable oxidation state of
132 Cr (Gunnewiek et al., 2014). Doping in metal oxide within certain limit of metal ions, serves to
133 increase stability, absorption of light and increase the charge carrier lifetime. Among metal ions,
134 rare earth (RE) metals have high conductivity and high thermal stability due to their
135 incompletely occupied 4f and empty 5d orbitals (Peng et al., 2017). Doping of RE ions, with the
136 metal oxide semiconductor materials is an effective method to enhance their photocatalytic
137 activities because RE ions can act as an electron trap. That, suppressed the electron-hole pairs
138 (e^-/h^+) recombination which in turn enhanced the destruction of recalcitrant organic pollutant in
139 wastewater (Xiao et al., 2008). Among the most widely used RE metals, samarium (Sm) is an
140 excellent candidate as dopants. Due to its nontoxicity, low price, good stability, ability to control
141 the chelation of Sm intermediate in the transition state and high efficiency in improving
142 photocatalytic activity (De la Cruza et al., 2011). It has been observed that the photocatalytic
143 activity enhanced with the increased of Sm concentration in the Sm doped ZnO due to the
144 existence of Sm(III)/Sm(II) sites. That, can act as an electron-hole trap centers, thus, retarded the
145 recombination rate (Sin et al., 2013). It has been found that the doping of ZnO nanoparticles with

146 Sm significantly improved its photocatalytic activity by 6.98 times compared to undoped ZnO
147 and increased absorption in the visible area for methylene blue degradation (Sukriti et al., 2020).
148 More recently, multi-walled carbon nanotubes (MWCNTs) have attracted great attention as
149 promising nanoparticles, and they have been seriously taken into consideration in fundamental
150 research and technological development. MWCNTs have been widely used in semiconductor
151 photocatalysts application. They possess unique nanostructures and significant properties, such
152 as novel electrical and mechanical properties, optical properties, high surface area, with
153 favourable thermal stability (Milne et al., 2014). In addition, it has excellent electron-carrying
154 capability leading to the enhanced photocatalytic performance (Iijima, 1991; Jitianu, 2004).
155 The presence of MWCNTs in BiVO₄/Bi₂WO₆/MWCNTs composite, narrowed the band gap,
156 improved the specific surface area, and avoided the agglomeration of nanocomposites.
157 Furthermore, increase the lifetime of charge carriers by suppressed the rate of recombination of
158 (e⁻/h⁺) pairs resulting in enhanced photocatalytic efficiency in wastewater treatment (Lin et al.,
159 2019). However, to the best of our knowledge, there is no article that has been published yet on
160 the study MWCNTs decorated doping of rare earth ions particularly Sm(III) in Cr₂O₃ and their
161 sonophotocatalytic performance under visible light irradiation. Herein, Sm-Cr₂O₃/MWCNTs was
162 successfully fabricated with uniform morphology via a simple hydrothermal route and
163 characterized by XRD, Raman, FTIR, SAED, SEM, EDS, TEM, HRTEM, DRS, BET and XPS
164 for the first time. The efficacy as a heterogeneous Fenton-like catalyst for (MET) abatement in
165 the presence of ultrasonic, visible light, and dual irradiation with H₂O₂ was tested. Moreover, the
166 effect of different lumped parameters was optimized for instance; irradiation time, catalyst dose,
167 H₂O₂ initial concentration pH, the mineralization and reusability were investigated. Furthermore,
168 experimental with addition of specific scavengers to understand contributions of the different

169 reactive species and reaction pathway were carried out. In addition, the possible mechanism with
170 pathways of MWCNTs supported Sm doped Cr₂O₃, the synergistic effect with reaction kinetics
171 was evaluated and identification of degraded intermediates was discussed.

172 **2. Experimental**

173 *2.1. Materials*

174 The drug (±)-Metoprolol(+)-tartrate salt, ≥99%, ammonia solution (25%), chromium (III) nitrate
175 nonahydrate Cr(NO₃)₃.9H₂O, nitric acid (70%), samarium(III) nitrate hexahydrate
176 Sm(NO₃)₃.6H₂O, sodium hydroxide, multi-walled carbon nanotubes (MWCNTs) >90% carbon
177 basis, with D x L (110–170 nm x 5–9 μm), hydrogen peroxide (30%, w/v) and ethanol were
178 purchased from Sigma Aldrich. Milli-Q-highly purified water system prepared in the laboratory
179 and was used throughout all experiments.

180 *2.2. Synthesis of catalysts*

181 *2.2.1. Synthesis of chromium sesquioxide (Cr₂O₃) nanoparticles*

182 Cr(NO₃)₃.9H₂O (0.1M) was dissolved in 100 mL of deionized water (D.I) for 30 min under
183 constant stirring. After that, ammonia solution was added drop wise under continuous stirring
184 until pH reached to 10.5. The reaction mixture was then transferred to a Teflon- sealed autoclave
185 and hydrothermally aged at 150°C for 17 h (Abdullah et al., 2014). A green flocculent precipitate
186 was recovered through centrifugation, washed repeatedly using D.I water, finally with ethanol
187 and subsequently dried at 70°C for 4 h. Finally, the Cr₂O₃ nanoparticles were formed after
188 calcination in air with the heating rate of 5°C/min at 800°C for 2h.

189 *2.2.2. Synthesis of Sm doped Cr₂O₃ nanoparticles*

190 Cr(NO₃)₃.9H₂O (5.0 mmol) and Sm(NO₃)₃.6H₂O (2.0 mmol) were added in 80 mL of D.I water.
191 Next, NaOH (30 mmol) was slowly added drop wise under strenuous stirring to this solution.

192 Then, the obtained slurry was kept under sonicated treatment for 30 min, followed by continuous
193 stirring for 3 h under ambient temperature conditions. After stirring, the resultant precipitate was
194 accumulated with centrifugation, repeatedly washed with D.I water and ethanol, to remove the
195 impurities, and subsequently dried at 70°C for 12 h. Calcination was performed at 800°C for 2 h
196 for the dried powder.

197 *2.2.3. Synthesis of MWCNTs/Sm -Cr₂O₃ nanocomposite catalyst*

198 Due to the MWCNTs stability, it should be oxidized before preparing the MWCNTs/ Sm -Cr₂O₃
199 composites, with strong acids to introduce active function groups on their surface. MWCNTs
200 were oxidized by refluxing with 70 wt% HNO₃ at 180°C under stirring conditions. Followed by
201 several times rinsing with D.I water on a sintered glass filter. Finally, vacuum-dried at 100°C for
202 5 h to obtain oxidized MWCNTs.

203 The MWCNTs/Sm-Cr₂O₃ nanocomposite catalyst was prepared by dispersed a certain amount of
204 oxidized MWCNTs and Sm/Cr₂O₃ in 25 mL ethanol and sonicated at 60 °C for 50 min followed
205 by vacuum drying at 70°C for 12 h.

206 *2.3. Characterizations of the catalyst*

207 X ray diffraction (XRD) analysis were carried out to assess the purity and the crystallite structure
208 of the prepared catalysts on a PANalytical diffractometer with Cu K α radiation ($\lambda = 1.54 \text{ \AA}$) in
209 the 2θ range of 20–80° with scanning speed 2° min^{-1} at 40 kV and 40 mA. Infrared (IR) spectra
210 were recorded on a Bruker Platinum ATR VERTEX 70v FT-IR Spectrometer. Raman analysis
211 was conducted at room temperature using a Horiba, LabRam HR Evolution with a 514.5 nm
212 green laser. TEM images, HRTEM and SAED were analysed using TEM on A JEOL, JEM-2010
213 (HT) at 200 kV. Morphology of the prepared catalysts were measured by SEM using a Hitachi S-
214 4800, equipped with (EDS) for further structural and elemental mapping of catalysts. The mass

215 titration method (Franca et al., 2009) was performed for the prepared catalysts to determine the
216 point of zero charge (pH_{PZC}) values. The presence of reactive oxygen species (ROS) were
217 recorded by radicals trapping agent 5,5-dimethyl-pyrroline-N-oxide (DMPO) and 2,2,6,6-
218 tetramethylpiperidine (TEMP) on EPR spectroscopy, using EPR, Adani CMS 8400 with 9.5 GHz
219 frequency. The absorption profiles and energy band gap (E_g) of the prepared catalysts were
220 measured by DRS on Agilent Cary 5000 UV-Vis spectrometer equipped with a DRA 2500
221 integrating sphere, using BaSO_4 as a reflectance standard. Compositions, chemical state, and
222 valence band position of the samples were measured by X-ray photoelectron spectroscopy
223 (XPS), using an ESCALAB 250Xi with Al-K α monochromatized radiation at 1486.6 eV.

224 *2.4. Sonophotocatalytic performance*

225 Ultrasonic irradiation, were emitted from a commercial sonicator, attached with a titanium alloy
226 probe with a tip diameter of 13 mm. Operated at fixed frequency (20 kHz) with a variable output
227 power of 125 W (Sonics& Materials, Model: VCX 750). During all the sonocatalytic run, a
228 thermocouple placed inside the reactor was used to monitor the temperature. The ultrasonic tip of
229 the probe was immersed below the surface of the MET solution about 2 cm during the
230 irradiation. All the experiments were performed in a double jacket quartz reactor of 110 mL
231 capacity attached with a circulating cooling water system to keep the temperature at $25 \pm 2^\circ\text{C}$.
232 For light irradiation a xenon lamp (MAX-350, Asahi Spectra Co., Ltd.) equipped with a VIS
233 mirror module (385–470 nm; Asahi Spectra Co. Ltd.) was placed in position above the quartz
234 double jacket reactor. During the sonocatalysis experiments, the light source was turned off,
235 while, during the photocatalysis experiments, sonicator was turned off. During the photocatalytic
236 runs a magnetic stirrer at 500 rpm was used to ensure adequate mixing of the suspension. In
237 addition, both the US/UV irradiation sources were simultaneously performed during the

238 sonophotocatalytic experiments. The suspension was circulated for 30 min in dark before
239 irradiation, to establish the adsorption–desorption equilibrium. For each catalytic run, a certain
240 amount of the prepared catalyst was dispersed into 110 mL MET solution. The reaction was
241 initiated after the rapid addition of H₂O₂ to MET solution and the US, Vis or US/Vis
242 immediately turned on. 1 mL of sample was collected from the reaction solution at regular time
243 interval filtered through regenerated cellulose (RC) membrane-syringe filters of 0.2 µm pore
244 size. HPLC, SHIMADZU® with a UV detector at wavelength of 220 nm attached with
245 Phenomenex® C18 column (5 µm, 150 mm × 4.6 mm) was used to measure the concentration of
246 samples. A mixture of 10 mM monobasic potassium phosphate solution and methanol (60:40 by
247 v/v) as the mobile phase was filtered through 0.22 Millipore membrane filter with 1 mL/min
248 flow rate before being used during the analysis. TOC analysis for the mineralization was carried
249 out using (TOC-VCPH Shimadzu) attached with (ASI-V-Shimadzu) auto sampler with TOC-V
250 series analyzer. All the experiments were performed triplicates to ensure system's reproducibility
251 and the error was calculated as standard deviation average ±.

252 **3. Results and discussion**

253 *3.1. Characterization of the catalyst samples*

254 *3.1.1. X ray diffraction pattern analysis*

255 Phase purity and crystal structure of the synthesized catalysts viz, Cr₂O₃, Sm- Cr₂O₃/ MWCNTs
256 and oxidized MWCNTs were displayed in XRD patterns, Fig.1. The XRD pattern of oxidized
257 MWCNTs revealed the appearance of the diffraction peaks at 2θ=25.83, 43.00, 44.99, 55.0 and
258 77.44, respectively that correspond to reflections of (002), (100), (101) (004) and (110) planes of
259 MWCNTs of the hexagonal graphite structure (JCPDS Card No.75-1621) (Chamssedine et al.,

260 2007). The XRD pattern of Cr₂O₃ shows all the diffraction peaks that confirm the rhombohedral
261 crystal structure, (Eskolaite) phase of Cr₂O₃ in accordance with (JCPDS Card No.38-1479). No
262 impurity peaks were detected in in Cr₂O₃ pattern, confirming the synthesis of highly pure Cr₂O₃
263 with well crystalline structure. The XRD pattern of Sm(III) doped Cr₂O₃ reveals that no
264 diffraction peaks of Sm were detected. Which indicates that Sm(III) ions are equally replacing
265 the Cr(III) sites of Cr₂O₃ crystal lattice or inserts and disperses homogenously into the crystal
266 lattice of Cr₂O₃. Thus, the decrease in the diffraction peaks intensities were observed because of
267 Sm doping Cr₂O₃ lattice. Since Sm(III) ions have a larger radius 0.0959 nm than Cr(III) ions
268 0.0615 nm. The XRD pattern of Sm-Cr₂O₃/MWCNTs exhibits all characteristic peaks of both
269 MWCNTs and Sm-Cr₂O₃, with slight decrease in peaks intensities and slight shift in peak
270 positions due to contraction of the lattice which suggests the formation of composites
271 nanoparticles. The average crystallite sizes of Cr₂O₃, Sm(III) doped Cr₂O₃ and Sm-
272 Cr₂O₃/MWCNTs were 27, 43 and 83 nm, respectively were calculated based on the Scherrer's
273 equation. Decrease in the crystal size of doped materials than Cr₂O₃ attributed to the formation of
274 Sm-Cr₂O₃ on the surface of the doped materials and the segregation of Sm ions at the grain
275 boundary of Cr₂O₃, which retards the growth of crystal grains with controlling direct contact of
276 crystal grains (Anandan et al., 2007; El-Bahy et al., 2009).

277 3.1.2. Infrared spectral analysis

278 To gain an understanding the functional group of the prepared samples, FTIR spectroscopy was
279 performed. The FTIR spectra of the oxidized MWCNTs, Cr₂O₃ and Sm-Cr₂O₃/MWCNTs are
280 displayed in Fig.2. The FTIR spectra show broad bands appear at 1620 and 3425 cm⁻¹
281 corresponding to the OH stretching vibration of the absorbed water molecules. A band at 1740
282 cm⁻¹ is assigned to the carboxylic (C=O) group attached to MWCNTs due to oxidation. The

283 respective bands appeared at 1428 and 2362 cm^{-1} are ascribed to C–H bending vibration and C–
284 O bonds. The absorption bands at 2855 and 2922 cm^{-1} are attributed to C–H stretching vibration
285 of methylene group generated from defects sites on the surface of MWCNTs by the acid
286 oxidation treatment (Singh et al., 2015). The FTIR spectrum of Cr_2O_3 shows bands that appeared
287 at 620 and 510 cm^{-1} are assigned to the rhombohedral Cr_2O_3 structure (Anandan et al., 2014).
288 The spectrum of the Sm doped Cr_2O_3 and Sm- Cr_2O_3 /MWCNTs clearly show that a slight shift in
289 the intensity of the absorption band position, towards the lower wave number after Sm doping,
290 assigned to the change in the bond length (Taylor, 1988; Faraz et al., 20018) and the formation
291 of Sm- Cr_2O_3 . However, the characteristic absorption bands of the MWCNTs are obviously
292 disappearance which suggests that the surface of MWCNTs has been covered by Sm- Cr_2O_3 .

293 3.1.3. Raman analysis

294 To probe the phase composition in the treated MWCNTs, Cr_2O_3 and Sm- Cr_2O_3 /MWCNTs;
295 further investigations using Raman analysis were performed, as presented in Fig.3. The Raman
296 spectrum of MWCNTs exhibits two strong peaks in the regions 1336 cm^{-1} called (D-band) and
297 1576 cm^{-1} called (G-band), are attributed to the disordered in the carbon nanotubes wall and the
298 in-plane vibration of the C–C bonded carbon atoms in graphene-like structures, respectively
299 (Pourfayaz et al., 2014). This result indicates that the graphitic structure of CNTs was not
300 destroyed during oxidation. Raman spectrum of Cr_2O_3 exhibits five Raman modes at about 307,
301 350, 386, 549 and 602 cm^{-1} , respectively corresponding to Raman modes of Cr_2O_3 (Yu et al.,
302 2003). A sharp and strong vibrational peak intensity of Raman band at 549 cm^{-1} is assigned to
303 the A_{1g} mode, belonging to the Cr–O stretching vibration of Cr^{3+} ions in octahedral
304 coordination. Thus, confirming the rhombohedral Cr_2O_3 structure with a high degree of
305 crystallinity (Mougina et al., 2001). However, the broad peaks at 307 cm^{-1} and 349 cm^{-1} are

306 assigned to the E_g vibration mode. These results are in accord with the previous reports (Larbi et
307 al., 2017). The Raman spectrum of Sm-Cr₂O₃/MWCNTs displays all the characteristic bands of
308 Cr₂O₃ and MWCNTs. Moreover, the peaks are broadened with a slightly shift of Raman band to
309 lower wave numbers, and the intensity of the Sm-Cr₂O₃ peaks is slightly increased, due to the
310 formation of the composites. While the MWCNTs peaks is disappeared after covering with the
311 Sm-Cr₂O₃, according to the formation of Sm-Cr₂O₃/MWCNTs composite. This is consistence
312 with FTIR results.

313 *3.1.4. SEM - EDS Analysis*

314 To analyze surface morphologies of the oxidized Cr₂O₃, MWCNTs, and Sm-Cr₂O₃/MWCNTs
315 were studied by SEM analysis as shown in Fig.4(a-d). The SEM image of Cr₂O₃ displays a
316 uniform near rhombohedral shapes with smooth surfaces Fig.4(a). While the SEM image of the
317 oxidized MWCNTs exhibits smooth, straight, and uniform tube walls 4(b). It is worth
318 mentioning that acid treatment did not deteriorate the structural integrity of MWCNTs. The SEM
319 image of Sm-Cr₂O₃/MWCNTs shows that the Sm-Cr₂O₃ nanoparticles are well dispersed along
320 the sidewall of the MWCNTs Fig.4(c,d). The chemical compositions and the distribution of the
321 elements in the Sm-Cr₂O₃/MWCNTs were scanned by EDS analysis and EDS elemental
322 mapping of the selected area in Fig. 4(e-j). The presence of Cr, O, Sm and C confirmed the
323 existence of Sm-Cr₂O₃ on the MWCNTs.

324 *3.1.5. TEM, HRTEM and SAED analysis*

325 To obtain more persuasive proof in shape, size and crystal structure of the prepared catalysts
326 TEM, HRTEM and SAED were performed. The TEM micrographs of the treated MWCNTs,
327 Cr₂O₃ and Sm-Cr₂O₃/MWCNTs were manifested at Fig.5(a-c). TEM image of oxidized
328 MWCNTs shows tubular structural morphology with average diameter of 70-85 nm and the

329 nanotubes length of 100 nm to several micrometers Fig.5(a). Whereas, Cr₂O₃ shows a uniform
330 near rhombohedral shapes with average particle size of 25-35 nm, which agree with crystallite
331 sizes data calculated by Scherrer's equation Fig.5(b). TEM image of Sm-Cr₂O₃/MWCNTs
332 clearly shows that the homogenous Sm-Cr₂O₃ nanoparticles are dispersed uniformly and
333 homogeneously over the surface of MWCNTs Fig.5(c). In addition, a strong attachment of Sm
334 doped Cr₂O₃ nanoparticles on MWCNTs surface enhances the photocatalytic activity due to
335 increases the number of active sites. The HRTEM image shows typical MWCNTs decorated
336 with Sm-Cr₂O₃ nanocrystal is illustrated in Fig.5(d). The lattice fringe spacing of Cr₂O₃ is 0.26
337 and 0.36 nm, which match to (104) and (012) the interplanar spacing for crystal plane of Cr₂O₃-
338 eskolaite. Whilst, the lattice fringes of 0.344 nm correspond to the (002) crystalline plane of the
339 MWCNTs wall. The corresponding SAED pattern of Sm-Cr₂O₃/MWCNTs shows the existence
340 of single crystalline phase of Cr₂O₃ as presented in Fig.5(e). The presence of spotty ring pattern
341 endorses the crystalline nature of Sm-Cr₂O₃/MWCNTs nanocomposites. Thus, TEM HRTEM
342 and SAED analysis explicitly validates the formation of Sm-Cr₂O₃/MWCNTs nanocomposite.

343 3.1.6. XPS analysis

344 To obtain further investigate of the oxidation states sensitivity and surface composition of the
345 prepared Sm-Cr₂O₃/MWCNTs, XPS analysis before and after the dual irradiation system was
346 performed in Fig.6 (a,b). The presence of the peaks of Cr, O, Sm, and C has been shown in the
347 XPS survey spectrum of Sm-Cr₂O₃/MWCNTs before dual irradiation performance was presented
348 in Fig.6(a). The Cr peaks located at 586.4 and 577.4 eV are assigned to the Cr 2p_{1/2} and Cr 2p_{3/2}
349 respectively, which is consistent with that of Cr³⁺ (Rahman et al., 1995). The observed peak
350 located at 530.43 eV is attributed to O 1s. The peaks are appeared at 1083.7 and 1109.7 eV, is
351 attributed to Sm 3d_{5/2} and Sm 3d_{3/2} signals of Sm³⁺ state, which is in accordance with the binding

352 energy in Sm_2O_3 (Lixi et al., 2015). The C 1s binding energy of the MWCNTs at 284.7 eV (Yan
353 et al., 2006), is assigned to the peak of graphitic carbon from MWCNTs. The results endorse that
354 the $\text{Sm-Cr}_2\text{O}_3/\text{MWCNTs}$ is stable and can catalyze oxidation- reduction cycles in the presence of
355 H_2O_2 to produce $\cdot\text{OH}$ under visible light irradiation. XPS spectra of the $\text{Sm-Cr}_2\text{O}_3/\text{MWCNTs}$
356 nanocomposite after dual irradiation performance are displayed in Fig.6(b).The XPS spectra
357 before and after dual irradiation performances display that, there are some of evident changes in
358 the intensity and in the shape of the peaks with a slight shift in the peak position. This finding
359 suggests to the presence of $\text{Cr}^{3+}/\text{Cr}^{6+}$, $\text{Sm}^{3+}/\text{Sm}^{2+}$ cycles in $\text{Sm-Cr}_2\text{O}_3/\text{MWCNTs}$ composite,
360 without obvious change in the composition and valance states in the XPS results. These changes
361 reveal that through heterogeneous Fenton like mechanism, ($\cdot\text{OH}$) are generated. Based on the
362 above XPS results are consistent with EDS results.

363 *3.1.7. DRS analysis*

364 The light absorption properties of the Cr_2O_3 , $\text{Sm-Cr}_2\text{O}_3$ and $\text{Sm-Cr}_2\text{O}_3/\text{MWCNTs}$, UV-visible
365 diffuse reflectance spectroscopy (DRS) was performed in the range of 250–800 nm to investigate
366 the optical properties, shown in Fig.7(a). Cr_2O_3 shows strong absorption of UV with an
367 absorbance edge of 360 nm, but weak absorption of visible light. While the absorption spectrum
368 of Sm doped Cr_2O_3 exhibit strong absorption in the visible-light range with a shift of the
369 absorption edge around 650 nm. This shift can be attributed to the charge transfer transition
370 between Sm ion 4f level electrons and Cr_2O_3 conduction band or valence band. Compared with
371 $\text{Sm-Cr}_2\text{O}_3$ the light absorption ability of the $\text{Sm-Cr}_2\text{O}_3/\text{MWCNTs}$ nanocomposite is significantly
372 enhanced with a slight shift in the visible range due to incorporation of MWCNTs (Lin et al.,
373 2016). The band gap energy (E_g) can be calculated from the intercept of the straight-line portion
374 of the plot of the modified Kubelka–Munk function $[F(R_\infty)/hv]^{1/2}$ versus (hv) the energy of the

375 absorbed light (Zhou et al., 2016). A plot of the modified Kubelka–Munk function versus the
376 energy of photon energy as displayed in Fig.7(b) affords the estimated value of band gap
377 energies (E_g) for Cr_2O_3 , $\text{Sm-Cr}_2\text{O}_3$ and $\text{Sm-Cr}_2\text{O}_3/\text{MWCNTs}$ were evaluated to be 3.30, 2.40,
378 and 2.10 eV, respectively. It is worth mentioning that, the narrower the band gap, higher
379 photocatalyst activity. These results indicate that the $\text{Sm-Cr}_2\text{O}_3/\text{MWCNTs}$ nanocomposite can
380 absorb the visible light in the UV as well as the visible regions and narrow the band gap. These
381 results suggested that the $\text{Sm-Cr}_2\text{O}_3/\text{MWCNTs}$ nanocomposite can be applied for the removal of
382 recalcitrant pollutant as a visible light photocatalyst. Thus, we univocally conclude the successful
383 formation of the $\text{Sm-Cr}_2\text{O}_3/\text{MWCNTs}$ nanocomposite, because of the XRD, FTIR, Raman, SEM,
384 EDS, elemental mapping TEM, HRTEM, SAED, XPS and DRS studies.

385 *3.2. Screening of US or Vis-light irradiation capabilities in MET degradation*

386 *3.2.1. MET degradation using sonolysis or photolysis catalytic system*

387 The effect of either US or Vis-light irradiation alone was screened in absence of any catalyst or
388 any promoter to estimate the effectiveness of the capability of the US or Vis-light irradiation for
389 the extent of MET degradation. As shown in Fig. S1. the obtained data reveal that the extent of
390 degradation after 60 min. was only 17 and 10%, for US and Vis respectively. The low efficiency
391 of US or Vis-light irradiation is attributed to the generation of different reactive radicals
392 generated during the sonolysis (within both extreme pressure and temperature) or photolysis
393 (attributed to the photolysis of water). Induces the generation of a considerable amounts of free
394 radicals such as $\cdot\text{OH}$ and $\text{H}\cdot$, which can generate other reactive oxygen species (ROS) (Petrier et
395 al., 1994). The hydroxylation reaction undergoes through the reaction of organic compounds by
396 the generated radicals and moreover through oxidation reaction in presence of air or oxygen
397 (Henglein, 1995; Tauber et al., 1999). However, the rate constant (K) value for the reaction of

398 oxygen and hydrated electrons (e_{aq^-}) and that between e_{aq^-} and MET and the tartrate ion is $1.9 \times$
399 $10^{10} \text{ M}^{-1} \text{ s}^{-1}$, $6.8 \times 10^7 \text{ M}^{-1} \text{ s}^{-1}$ and $1.7 \times 10^7 \text{ M}^{-1} \text{ s}^{-1}$, respectively. While the rate constants for
400 two hydroxyl radicals combination and for the reaction of $\cdot\text{OH}$ react with MET and the tartrate
401 ion is $5.2\text{--}6.2 \times 10^9 \text{ M}^{-1} \text{ s}^{-1}$, $5.2 \times 10^9 \text{ M}^{-1} \text{ s}^{-1}$ and $5.5 \times 10^8 \text{ M}^{-1} \text{ s}^{-1}$, respectively (Slegers et al.,
402 2003). Although, (K) value for combination of two $\cdot\text{OH}$'s is lower than that for the reaction
403 between MET and the tartrate ion with $\cdot\text{OH}$, there exists a considerable loss of the generated $\cdot\text{OH}$
404 and e_{aq^-} which takes place before participation in MET degradation process. That interprets
405 limited the efficiency of sonolysis alone under the used conditions. Also, the obtained data reveal
406 that the extent of degradation after 60 min with photolysis alone was insignificant and the
407 produced amounts of $\cdot\text{OH}$'s were not enough for complete degradation of MET. The effect of
408 different H_2O_2 concentration using sonolysis and photolysis irradiation in the range of 10–80mM
409 was investigated, in Fig. S2. The degradation extent at 40mM H_2O_2 reached 33% and 50% under
410 US and Vis-light irradiation respectively, while the degradation extent at 60mM H_2O_2 reached
411 11% and 23% under US and Vis-light irradiation respectively. Thus, the degradation extent
412 decreased with more increase in H_2O_2 amount further on this concentration. The enhancement
413 for the degradation efficiency upon the addition of H_2O_2 is due to enrichment in the production
414 of hydrogen peroxide radicals (Beltran, 2003; Voigt et al., 2021). Furthermore, the bond energy
415 between O–O (139 kJ mol^{-1}) in H_2O_2 cleavage much easier than that of the bond energy
416 between O–H (463 kJ mol^{-1}) of water (Mehrdad and Hashemzadeh, 2010). While, the free
417 radicals generated were scavenging instead of producing additional radicals upon the addition of
418 the extra amount of hydrogen peroxide. Recognized as the scavenging phenomenon of $\cdot\text{OH}$,
419 ultimately the degradation efficiency decreases (Panda and Manickam, 2017; Abbasi and Asl,
420 2008).

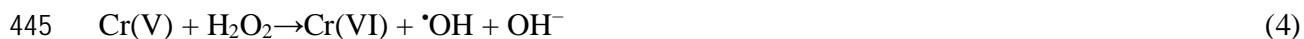
421 *3.2.2. Effect of ultrasonic or photo-heterogeneous Fenton*

422 The degradation efficiency of MET, in silent mode without US or Vis-light irradiation were
423 performed, to probe the capability of Sm-Cr₂O₃/MWCNTs. It can be seen that the degradation
424 efficiency reached 15% using 80mM of H₂O₂, 0.1 g L⁻¹ of the catalyst, MET (10 mgL⁻¹) at pH 7
425 and after 60 min of stirring. Thus, the degradation efficiency decreases as the result of the
426 turbulence of the solution.

427 *3.2.2.1. Effect of sonocatalytic or photocatalytic irradiation time.*

428 The sonocatalytic and/or photocatalytic degradation of MET (10 mgL⁻¹) at 80mM of H₂O₂ in
429 presence of 0.3 g L⁻¹ of Sm-Cr₂O₃/MWCNTs nanocomposite and pH = 7 at room temperature,
430 the effect of irradiation time was investigated after 60 min time for irradiation. The results
431 showed that the degradation efficiency has been increased remarkably to 77 and 84% for US and
432 Vis-light, respectively as displayed in Fig. S3. The higher degradation performance resulted on
433 adding H₂O₂ to US can be attributed to excessive generation of [•]OH due to the metal -induced
434 H₂O₂ decomposition at the solid liquid interface wherein highly reactive oxygen species are
435 generated through a redox cycle. Based on the heterogeneous Fenton-like reaction using
436 chromium oxide, the reaction between Cr(III) and H₂O₂ generates chromium species Cr(IV) as a
437 synchronous intermediate (Tsou and Yang, 1996). Instantly, Cr(IV) species are able to generates
438 Cr(V) species as reactive chromium intermediates (Shi and Dalal, 1990). Which are able to
439 generate a considerable numbers of [•]OH due to a series of reactions with H₂O₂ (Shi et al., 1993)
440 follows a sequential Fenton-like pathway as is illustrated in the following equations (Bokare and
441 Choi, 2011):





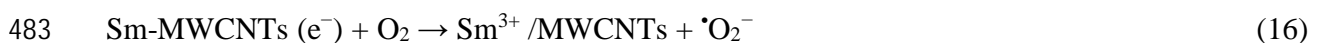
446 According to the above equations, the transformation of Cr(III) into Cr(VI) via redox cycle in the
447 Cr(III)/Cr(VI)-H₂O₂ system generates $\cdot\text{OH}$, Cr(IV) and Cr(V) species, as active intermediate
448 through Fenton-like reactions.

449 On the other hand, the addition of MWCNTs in Sm-Cr₂O₃/MWCNTs increased the adsorption
450 ability of the catalysts due to the dispersion of the catalyst on the nanotubes. In addition,
451 MWCNTs increased particle fragmentation, cavitation bubbles and consequently increased
452 induction of hot spots, through the heterogeneous nucleation of bubbles, which can cause
453 pyrolysis of water molecules to produce hydroxyl radicals under US irradiation (Zhang et al.,
454 2011). The higher catalytic activity of Sm-Cr₂O₃/MWCNTs under Vis-light irradiation can be
455 attributed to accelerate the charge transfer due to doping of Sm on Cr₂O₃ which resulted in the
456 increase in $\cdot\text{OH}$ formation. When the catalyst is irradiated with Vis-light, the electron e⁻ is
457 excited from the valance (VB) band to the conduction band (CB), leaving holes (h⁺) in the VB of
458 Cr₂O₃. The (e⁻) in the CB reacts with the Sm³⁺ in order to that it is a strong lewis acid that has
459 partially filled 4f orbital which can trap the e⁻ and suppress the recombination of charge carrier,
460 thus enhancement of their lifetime. Consequently, the unstable form of Sm⁺² ions is formed, that
461 has the tendency to transfer the e⁻ to O₂, to form $\cdot\text{O}_2^-$ which form $\cdot\text{OOH}$ after protonation was
462 formed. Then it was converted to the $\cdot\text{OH}$. Simultaneously, h⁺ VB reacts with the water
463 molecules adsorbed on the catalyst surface and form hydroxyl radical. In addition, O₂ and H₂O
464 molecules act as scavengers to trap e⁻ and h⁺ to generate $\cdot\text{OH}$ species (Sin et al., 2013). Thus, the

465 generation of $\cdot\text{O}_2^-$ and $\cdot\text{OH}$ leads to the degradation of MET. The degradation mechanism for
 466 Sm-doped $\text{Cr}_2\text{O}_3/\text{MWCNTs}$ is shown in the following equations:



475 On the other hand, the addition of MWCNTs also, acts as an electron trap and is able to suppress
 476 the e-/h+ recombination (Zhao et al., 2017), with Sm because it can act as conductive to
 477 transferring and separation of exciting electrons as electron mediators. The e^- on the surface of
 478 Sm- Cr_2O_3 can be trapped and transferred quickly by the MWCNTs. The e^- on MWCNTs can
 479 react with O_2 to produce $\cdot\text{O}_2^-$ and $\cdot\text{OH}$ as displayed on the following equations.





486 Thus, Sm and MWCNTs dopants in Cr_2O_3 improved the photocatalytic degradation of MET due
487 to the separation of the charge carriers by trapping, resulted in increase in the generation of $\cdot\text{OH}$,
488 $\cdot\text{O}_2^-$ and h^+ from the two postulated mechanism.

489 3.2.2.2. *Effect of H_2O_2 addition*

490 The addition of H_2O_2 in the range of 10–80mM improves the degradation efficiency of MET up
491 to a definite amount of H_2O_2 , for US 40mM, and for Vis-light 50mM as display in Fig. S4. The
492 decomposition of H_2O_2 under US or Vis-light irradiation to produce hydroxyl radicals causes a
493 remarkable enhancement in degradation efficiency. Hydrogen peroxide dissociates to generate
494 hydroxyl radicals under US or Vis-light irradiation. However, it also, has the scavenger effects of
495 $\cdot\text{OH}$ by H_2O_2 with extravagant amounts of H_2O_2 . Which is capable to decrease the MET
496 degradation slightly. Thus, H_2O_2 plays a vital role in the enhancement or decline degradation
497 extent and is considered as highly relevant in the catalytic degradation domain (Pham et al.,
498 2018). Moreover, the addition of H_2O_2 also acts as an e^- trap and can increase separation ability
499 of (e^-/h^+) pairs (Malato et al., 2000). The result showed that the Vis-light irradiation improves
500 the generation of $\cdot\text{OH}$ more than US that endure the scavenging effect of H_2O_2 added up to
501 50mM.

502 3.2.2.3. *Effect of catalyst loading*

503 The amount of catalyst is considered as one of the main parameters for the degradation studies
504 from economical point of view. Therefore, it is necessary to avoid the use of excess catalyst and

505 find out the optimum loading for efficient degradation performance of MET. Various amounts of
506 the catalyst in the range of (0.1-1) g L⁻¹ of Sm-Cr₂O₃/MWCNTs were tested for US and Vis-light
507 irradiation on the degradation of MET as display in Fig.S5 .The results indicates that the 0.3 g
508 L⁻¹ is the optimum catalyst amount for the degradation of MET. Further increase in the catalyst
509 amount, the degradation efficiency begins to decrease slowly. The aggregation of Sm-
510 Cr₂O₃/MWCNTs particles causing decrease in the surface active sites number and increase in the
511 opacity and light scattering of the particles at high concentration. Which in turn, decrease in the
512 irradiation path through the sample at high concentrations (Kaur and Singh, 2007).

513 *3.3. Optimization condition of sonophotocatalysis-Fenton system for the degradation of MET*
514 *using Sm-Cr₂O₃/MWCNTs nanocomposite.*

515 To identify the optimum parameters for the mineralization of MET; all the different
516 conditions of the sonocatalytic and photocatalytic processes were optimized and performed in the
517 dual irradiation system for the degradation of MET as illustrated in Fig.8. The results manifest
518 that the sonophotocatalytic system was capable to achieve total degradation of MET (10 mg/L)
519 after 50 min of dual irradiation US/UV using 0.3 g L⁻¹ of the Sm-Cr₂O₃/MWCNTs in the
520 exitance of 50 mM H₂O₂ and pH = 7. The sonophotocatalytic degradation efficiency was higher
521 compared to the individual sono or photocatalytic degradation or even their sum, which a
522 synergistic effect proved. The sonophotocatalytic degradation efficiency was higher than that of
523 the sonocatalytic or photocatalytic system by 26% and 20%, respectively with the extent of
524 degradation ordered sonophotocatalysis > photocatalysis > sonocatalysis. This remarkable
525 degradation performance can be ascribed to the simultaneous use of US and Vis-light irradiation.
526 Moreover, the presence of two sources of irradiations enhances the generation of hydroxyl
527 radicals, which eventually enhances sonophotocatalytic performance. However, the two major

528 factor induced synergy that contributes to the US were the deactivation of the catalyst and de-
 529 agglomeration. This causes removing adsorbed moieties from the surface via microstreaming and
 530 microbubbles eruptions (Anju et al., 2012). The synergy index was calculated from the rate
 531 constant of each systems under the identical conditions using the following Eq. (19) (Verma et
 532 al., 2013).

$$\begin{aligned}
 &533 \text{ Synergy (S\%)} = \frac{(\mathbf{k_{sonophotocatalysis}} - (\mathbf{k_{sonocatalysis}} + \mathbf{k_{photocatalysis}}))}{\mathbf{k_{sonophotocatalysis}} \quad \mathbf{X 100} \quad (19) \\
 &534 \\
 &535 \\
 &536
 \end{aligned}$$

537 The synergetic effect of sonophotocatalytic degradation was faster than the sole systems as
 538 depicted in Table 1 and in Fig.S6. Moreover, the results indicate that the dual irradiation system
 539 has a value greater than 1, indicating a positive synergistic effect on MET degradation
 540 performance.

541 3.3.1. Effect of initial pH

542 To investigate the effect of pH on the sonophotocatalytic system, a wide pH range of 3–11 was
 543 used to determine the applicability of the Sm-Cr₂O₃/MWCNTs for MET degradation in Fig.S7.
 544 The result indicates that MET degrade completely after 50 min in the presence of the Sm-
 545 Cr₂O₃/MWCNTs with US/Vis system through the extended pH range, even under acidic at pH=
 546 3 and basic (pH =11) conditions, attributed to the surface charge of the material (Romero et al.,
 547 2013). The p_{H_{ZPC}} values determined for MWCNTs, Cr₂O₃, and Sm-Cr₂O₃/MWCNTs were 4,
 548 7.6 and 6.8, respectively. The catalyst surface was positively charged, when the values of pH
 549 lower than p_{H_{ZPC}}, become negatively charge at pH higher than p_{H_{ZPC}}. Thus, under acidic
 550 conditions the catalyst surface was positively charged and the recombination rate of e⁻/h⁺ pairs
 551 was decreased providing a higher degradation rate of MET. Meanwhile, the surface was

552 negatively charged under basic conditions with the repulsive electrostatic effect between catalyst
553 surface and deprotonated MET (Ye et al., 2018). The pKa values of MET have been reported to
554 be 9.7 (Benitez et al., 2011; Jessica et al., 2021). This suggests that it can lose a proton from the
555 -OH group on the side chain and transformed into negatively charged anion form. The presence
556 of negative charges on the catalyst surface inhibits the sorption of OH^- ions and water molecules,
557 and consequently decreases the amount of $\cdot\text{OH}$ radicals formed and increasing the recombination
558 rate of the electrons generated in the CB with VB of the catalyst (Huerta Aguilar et al., 2015).
559 The same effect of alkaline pH in MET degradation has been reported and discussed by (Ye et
560 al., 2018; Habibi et al., 2005), where, the major MTP degradation occurred in the (bulk liquid
561 phase) and secondary occurred on catalyst surface (liquid interface). Which, involving either
562 direct oxidation by $\cdot\text{OH}$ adsorbed on the catalyst surface or photo generated h^+ . The high pH
563 induced repulsive effect of the catalyst surface towards deprotonated MTP molecules resulted in
564 inhibition of the secondary MTP degradation route. However, using the Sm-Cr₂O₃/MWCNTs
565 showed a remarkable achievement through the extended alkaline pH range and can be cover all
566 the alkaline pH range attributed to the relation between pH and Cr(VI)/Cr(III) and O₂/H₂O₂
567 couples. This demonstrate that H₂O₂ can oxidize Cr(III) at pH > 8 and reduce Cr(VI) at lower
568 pH. Since the reducing strength of H₂O₂ strongly increases with decreasing pH, the H₂O₂-
569 induced reduction of Cr(VI) to Cr(III) at pH < 3 is used for removing chromate from wastewaters
570 (Bokare and Choi, 2011).

571 *3.4. Trapping experiments of reactive species*

572 To investigate the sonophotocatalytic pathway with full understanding of the MET degradation
573 process over Sm-Cr₂O₃/MWCNTs, it is imperative to identify the leading active species using
574 the trapping experiments as display in Fig.9. In this study, a series of different concentration of

575 scavengers were selected to identify the major active species involved in the dual irradiation
576 system for MET degradation. We insert potassium dichromate to trap e^- , ethylene
577 diaminetetraacetic acid (EDTA) to trap (h^+), benzoquinone (BQ) to trap ($\cdot O_2^-$) and isopropanol
578 (IPA) to trap ($\cdot OH$). From the results manifested in Fig.9, it is apparent that the introduction of
579 (IPA), (EDTA) and (BQ), unveil a considerable decline in the sonophotocatalytic performance of
580 Sm-Cr₂O₃/MWCNTs for the degradation of MET. Nonetheless, the degradation extent of MET
581 slightly enhances with the addition of (e^-) trappers because trapping of the generated electrons
582 owing to increase the number of surviving h^+ . Thus, it can be deduced that the active species and
583 function major roles follow the order $\cdot OH > h^+ > \cdot O_2^-$ in the MET degradation with dual
584 irradiation system.

585 3.5. EPR spectroscopy

586 To determine the radicals produced while using Sm-Cr₂O₃/MWCNTs, photocatalyst under the
587 (US/Vis) irradiation system, EPR spectroscopic analysis was executed as shown in Fig.10(a,b).
588 DMPO and TEMP were used as spin trap for radical species. The EPR spectrum taken with
589 DMPO in the absence of Sm-Cr₂O₃/MWCNTs did not show any peaks in EPR spectra. Whereas,
590 four typical peaks were detected when Sm-Cr₂O₃/MWCNTs was added and their intensity
591 increases with irradiation time. Which indicates the formation of DMPO-OH adduct suggest the
592 generation of more $\cdot OH$ as shown in Fig.10(a). Thus, more free radicals would be generated as a
593 result of a good separation effect on photo-generated e^-/h^+ pairs (Wang et al., 2019) performed
594 by Sm-Cr₂O₃/MWCNTs. While, by adding the TEMP trapping agent, a triplet pattern of equal
595 intensity was indexed in Fig.10(b), indicates the presence of TEMP-¹O₂ adduct in EPR spectra
596 and confirms the formation of the singlet oxygen. Moreover, these characteristic peaks decreased
597 with time irradiation. It suggested that ¹O₂ radical generation was gradually exhausted through

598 direct participation in the degradation reaction under dual US/Vis irradiation systems with fast
599 reaction rate. EPR analysis clearly confirmed the production of $\cdot\text{OH}$ and $^1\text{O}_2$ radicals in MET
600 degradation by using Sm-Cr₂O₃/MWCNTs under US/UV system.

601 *3.6. Reusability*

602 The stability and recyclability of Sm-Cr₂O₃/MWCNTs is of supreme importance to explore as it
603 could reduce the cost of the catalytic process appreciably, thus, produce a promising catalyst for
604 the destruction of virulent organic pollutant. The sonophotocatalytic stability and reusability of
605 Sm-Cr₂O₃/MWCNTs throughout six successive runs under the same operating conditions is
606 presented in Fig.11. The sonophotocatalytic performance slightly decreased after six cycles. The
607 enhanced stability of Sm-Cr₂O₃/ MWCNTs toward MET degradation is attributed to the synergic
608 effect between Sm-Cr₂O₃ and MWCNTs. Furthermore, the sonophotocatalytic stability of the
609 Sm-Cr₂O₃/MWCNTs is also indicated by its XRD and SEM analyses data. There was no obvious
610 change in XRD patterns and morphology after the six successive runs of sonophotocatalytic
611 degradation of MET as illustrated in Fig. S8(a,b). Thus, the recycling results reflect the superior
612 stability and recyclability of the Sm-Cr₂O₃/MWCNTs nanocomposite with their applicable
613 potential for environmental applications.

614 *3.7. TOC and mineralization*

615 TOC measurements after complete MET removal, about 10% of organic compounds remained in
616 the system with the Sm-Cr₂O₃/MWCNTs as TOC measurements displayed. However, the
617 percentage of remaining organic compounds decreased to 4% after 120 min of dual US/Vis
618 irradiation systems, as shown in Fig.S9. The formed intermediates need longer time to be
619 completely mineralized, due to their slower rate of reaction with attacking $\cdot\text{OH}$ (Wang et al.,

620 1998). It is worth mentioning that, higher generation rate of $\cdot\text{OH}$ and $\cdot\text{O}_2^-$ and enhanced
621 performance of e^-/h^+ pairs is the remarkable effect in the sonophotocatalytic performance of the
622 Sm-Cr₂O₃/MWCNTs.

623 *3.8. Determination of intermediates and mechanism of photodegradation, determination of* 624 *intermediate degradation products by GC-MS*

625 To characterize all the degradation products formed under various stress conditions, Gas
626 chromatography – mass spectrometry GC–MS analysis was performed. Analyzing reaction
627 mixtures by GC-MS analysis, several intermediate aromatic compounds were identified. GC–MS
628 analysis of MET revealed the presence of three unique fragments (267, 107 and 71) (m/z) Fig S10
629 (a). While, the analysis of mixtures obtained after dual irradiation system US/Vis irradiation (50
630 min) allowed the identification of several new intermediate organic compounds as displayed in
631 Fig. S10 (b). Each peak was analyzed in each chromatogram to determine the molecular ion (M),
632 the characteristic fragmentation pattern and the retention time (min). The product was identified
633 by comparing the molecular ion and mass fragmentation pattern with those reported in the GC-
634 MS library. The MET has a molecular weight [M⁺] = 267.1. The identified intermediates allowed
635 for the proposal of a possible mechanism for MET degradation. Thus, the reaction pathway for
636 the degradation of (MET) includes the transformation of metoprolol to hydroquinone via the
637 cleavage of the C-O in the aryl ether to form 4-(2-methoxy ethyl) phenol. Then it is transformed
638 to form 2-(4-hydroxyphenyl) ethanol with consecutive hydroxylation. After that, it is oxidized to
639 form the 4-hydroxybenzaldehyde followed by transformed to hydroquinone (Pinedo et al., 2016).
640 Metoprolol is also degraded directly to hydroquinone. Then, this aromatic compound is oxidized
641 with further oxidation to 1,2,4-benzenetriol, which is rapidly oxidized to low molecular weight
642 organic acids before being completely mineralized to CO₂ and H₂O (Moctezum et al., 2013). The

643 photocatalytic degradation using a xenon lamp as irradiation source of β -blockers and MET as
644 model compound in an aqueous suspension of TiO_2 (Leyva et al., 2019) had the similar
645 mechanism (Romero et al., 2013). In this study two intermediates were detected at m/z 300, 332,
646 and 108 respectively, corresponding to 4-(2-methoxyethyl) phenyl and 4-[2-hydroxy-3-(propan2-
647 ylamino) propoxy] benzaldehyde (Abramović et al., 2011). Which regarding to the binding of
648 hydroxyl radicals in the aromatic ring and one for the hydrogen abstraction with elimination of
649 water to generate a carbonyl, followed by the loss of ammonia. Then after breaking of c-c bond
650 in the aliphatic part, amino-diol and the ethanolamine side are formed due to the loss of
651 isopropyl moiety and the hydroxyl group. Thus, the proposed mechanism of MET degradation
652 demonstrated that the same mechanism as previously studied (Song et al., 2008).

653 **Conclusion**

654 A successful synthesis via a facial hydrothermal route for Sm doped Cr_2O_3 decorated
655 MWCNTs. Optimum parameters for the degradation of MET with dual irradiation system were
656 identified in terms of H_2O_2 concentration, irradiation time, catalyst dosing and pH. Furthermore,
657 the photocatalytic performance enhancing by Sm doping which shifting the photogenerated
658 carriers to surface of photocatalyst and suppressing photoinduced charge recombination. The
659 absorption edge of the Sm- Cr_2O_3 /MWCNTs shifted to longer wavelength as compared to Cr_2O_3
660 which generating e^- and h^+ under Vis-light irradiation as display in the diffuse reflectance
661 spectra. A dual irradiation US/UV system for the degradation pathway of MET on the Sm-
662 Cr_2O_3 /MWCNTs were discussed based on the identified intermediates after 50 min.
663 Hydroxylation of the aromatic ring, by addition of $\cdot\text{OH}$ or cleavage of the amine lateral chain
664 followed by shortening of methoxy group in the lateral chain, is the main pathway for the
665 degradation process by dual irradiation system.

666 **Acknowledgement**

667 The authors wish to acknowledge the financial support of this research by MVTT grant in
668 Finland, as well as thankful to the department of separation science, School of Engineering
669 Science, LUT University, Mikkeli, Finland. In addition, Authors acknowledge the financial
670 support through Researchers Supporting Project number (RSP-2021/345), King Saud University,
671 Riyadh, Saudi Arabia.

672

673 **References**

- 674 [1] Richardson, M.L.; Bowron, J.M.; The fate of pharmaceutical chemicals in the aquatic
675 environment, *J. Pharm. Pharmacol.* **1985**, 37, 1–12, <https://pubmed.ncbi.nlm.nih.gov/2858520/>
- 676 [2] Verlicchi, P.; Al Aukidy, M.; Zambello, E.; Occurrence of pharmaceutical compounds in
677 urban wastewater: removal, mass load and environmental risk after a secondary treatment—A
678 review *Sci. Total Environ.* **2012**, 429, 123–155, <https://pubmed.ncbi.nlm.nih.gov/22583809/>
- 679 [3] Martínez, C.; Canle L, M.; Fernández, M.I.; Santaballa, J.A.; Faria, J. Aqueous degradation
680 of diclofenac by heterogeneous photocatalysis using nanostructured materials, *Appl. Catal. B:
681 Environ.* **2011**, 107, 110–118, <https://doi.org/10.1016/j.apcatb.2011.07.003>
- 682 [4] Santos, L.; Araújo, A.; Fachini, A.; Pena, A.; Deleure-Matos, C.; Montenegro, M.
683 Ecotoxicological aspects related to the presence of pharmaceuticals in the aquatic environment,
684 *J. Hazard. Mater* **2010**, 175, 45–95, <https://doi.org/10.1016/j.jhazmat.2009.10.100>
- 685 [5] Simazaki, D.; Kubota, R.; Suzuki, T.; Akiba, M. ; Nishimura, T.; Kunikane, S. Occurrence of
686 selected pharmaceuticals at drinking water purification plants in Japan and implications for
687 human health, *Water Research* **2015**, 76, 187–200, <https://pubmed.ncbi.nlm.nih.gov/25835589/>
- 688 [6] Isidori, M.; Bellotta, M.; Cangiano, M.; Parrella, A.; Estrogenic activity of pharmaceuticals
689 in the aquatic environment, *Environ. Int.* **2009**, 35, 826–829,
690 <https://doi.org/10.1016/j.jhazmat.2009.10.100>
- 691 [7] Chakraborty, S.; Loutatidou, S.; Palmisano, G.; Kujawa, J.; Mavukkandy, M. O.; Al-
692 Gharabliac, S.; Curciob, E.; Arafata, H. A. Photocatalytic hollow fiber membranes for the
693 degradation of pharmaceutical compounds in wastewater, *J. Environ. Chem. Eng.* **2017**, 5 (5)
694 5014–5024 <https://doi.org/10.1016/j.jece.2017.09.038>

- 695 [8] Marothu, Vamsi Krishna, Gorrepati , Madhavi, Nagi F.I dris, Salah Ali M. Idris, Lella. Ravi
696 Kiran Chowdary, Photocatalysis of β -blockers – An overview, Arabian Journal of Chemistry,
697 **2019**, 12, 7. 1290-1297, <https://doi.org/10.1016/j.arabjc.2014.10.044>
- 698 [9] Eike D., Marcus R., Dirk J.The Database “Pharmaceuticals in the Environment”-Update and
699 New Analysis, Umweltbundesamt; Dessau, Germany (Texte) **2019**, 67, 1-103
700 <http://www.umweltbundesamt.de/publikationen>
- 701 [10] Yang, H.; An, T.; Guiying Li, Song, W.; Cooper, W. J.; Luo, H.; Guo, X.; Photocatalytic
702 degradation kinetics and mechanism of environmental, pharmaceuticals in aqueous suspension of
703 TiO₂: A case of β -blockers, J. Hazard. Mater. **2010**, 179, 834–83,
704 <https://doi.org/10.1016/j.jhazmat.2010.03.079>
- 705 [11] Abramović, B.; Kler, S.; Šojić, D.; Laušević, M.; Radović, T.; Vione, D. Photocatalytic
706 degradation of metoprolol tartrate in suspensions of two TiO₂-based photocatalysts with
707 different surface area. Identification of intermediates and proposal of degradation pathways, J.
708 Hazard. Mater. 2011, **198**, 123–132, <https://doi.org/10.1016/j.jhazmat.2011.10.017>
- 709 [12] Alder, A.C.; Schaffner, C.; Majewsky, M.; Klasmeier, J.; Fenner, K.; Fate of b-blocker
710 human pharmaceuticals in surface water: comparison of measured and simulated concentrations
711 in the Glatt Valley Watershed, Switzerland, Water Res. **2010**, 44 (3), 936-948,
712 <https://pubmed.ncbi.nlm.nih.gov/19889439/>
- 713 [13] Gabet-Giraud, V.; Miege, C.; Choubert, J.M.; Ruel, S.M.; Coquery, M.; Occurrence and
714 removal of estrogens and beta blockers by various processes in wastewater treatment plants. Sci.
715 Total Environ. **2010**, 408 (19), 4257-4269, <https://pubmed.ncbi.nlm.nih.gov/20633734/>
- 716 [14] Xu, Y.; Nguyen, T. V.; Reinhard, M.; Gin, K. Y.-H.; Photodegradation kinetics of p-tert-
717 octylphenol, 4-tert-octylphenoxy-acetic acid and ibuprofen under simulated solar conditions in
718 surface water, Chemosphere, **2011**, 85 (5) 790–796, <https://pubmed.ncbi.nlm.nih.gov/21745677/>
- 719 [15] Wilde, M. L.; Montipó, S.; Martins, A. F.; Degradation of b-blockers in hospital
720 wastewater by means of ozonation and Fe²⁺/ozonation, Water Res. **2014**, 48, 280-295,
721 <https://doi.org/10.1016/j.watres.2013.09.039>
- 722 [16] Vieno, N.; Tuhkanen, T.; Kronberg, L.; Elimination of pharmaceuticals in sewage treatment
723 plants in Finland, Water Res., **2007**, 41(5), 1001-1012,
724 <https://doi.org/10.1016/j.watres.2006.12.017>
- 725 [17] Píram, A.; Salvador, A.; Verne, C.; Herbreteau, B.; Faure, R. ; Photolysis of β -blockers in
726 environmental waters, Chemosphere, **2008**, 73 (8) 1265–1271,
727 <https://doi.org/10.1016/j.chemosphere.2008.07.018>

- 728 [18] Molinari, R.; Pirillo, F.; Loddo, V.; Palmisano, L.; Heterogeneous photocatalytic
729 degradation of pharmaceuticals in water by using polycrystalline TiO₂ and a nanofiltration
730 membrane reactor, *Catal. Today*, **2006**, 118 (1-2), 205–213,
731 <https://doi.org/10.1016/j.cattod.2005.11.091>
- 732 [19] Song, W.; Cooper, W. J.; Mezyk, S. P.; Greaves, J.; Peake, B. M. ; Free radical destruction
733 of β -blockers in aqueous solution, *Environ. Sci. Technol.*, **2008**, 42 (4), 256–1261,
734 <https://doi.org/10.1021/es702245n>
- 735 [20] Romero, V.; Cruz, N.De la.; Dantas, Renato F.; Marco, P.; Giménez, J.; Esplugas, S.;
736 Photocatalytic treatment of metoprolol and propranolol, *Catal. Today* **2011**, 161 (1), 115-120,
737 <https://doi.org/10.1016/j.cattod.2010.09.026>
- 738 [21] Zainab Haider Mussa, Fouad Fadhil Al-Qaim, Ali Yuzir, Kamyar Shameli, Electrochemical
739 Degradation of Metoprolol Using Graphite-PVC Composite as Anode: Elucidation and
740 Characterization of New by-products Using LC-TOF/MS, *J. Mex. Chem. Soc* , **2020**, 64,3, 165-
741 180, <https://doi.org/10.29356/jmcs.v64i3.1139>
- 742 [22] Xiaoyong Yang, Rusen Zou, Kai Tang, Henrik Rasmus Andersen, Irini Angelidaki, Yifeng
743 Zhang, Degradation of metoprolol through bio-electro-Fenton in a bioelectrochemical system
744 (BES), *Science of the Total Environment*, **2021**, 771, 145385,
745 <https://doi.org/10.1016/j.scitotenv.2021.145385>
- 746 [23] Jessica Guadalupe Piedra López, Orlando Haciél González Pichardo, José Alfonso Pinedo
747 Escobar, David Alejandro de Haro del Río, Horacio Inchaurregui Méndez, Luis Mario González
748 Rodríguez, Photocatalytic degradation of metoprolol in aqueous medium using a TiO₂/natural
749 zeolite composite, *Fuel*, **2021**, 284, 119030, <https://doi.org/10.1016/j.fuel.2020.119030>
- 750 [24] Yu-qiong Gao, Jia Zhang, Cong Li, Fu-xiang Tian, Nai-yun Gao, Comparative evaluation of
751 metoprolol degradation by UV/chlorine and UV/H₂O₂ processes, *Chemosphere*, **2020**, 243,
752 125325, <https://doi.org/10.1016/j.chemosphere.2019.125325>
- 753 [25] Melanie Voigt, Indra Bartels, Dorothee Schmiemann, Lars Votel, Kerstin Hoffmann-
754 Jacobsen, Martin Jaeger , Metoprolol and Its Degradation and Transformation Products Using
755 AOPs—Assessment of Aquatic Ecotoxicity Using QSAR, *Molecules*, **2021**, 26, 11, 3102,
756 <https://doi.org/10.3390/molecules26113102>
- 757 [26] Osmín Avilés-García, Jaime Espino-Valencia, Arisbeht Mendoza-Zepeda, Kingsley
758 Donkor, Sharon Brewer, Rubi Romero, Reyna Natividad, Removal of metoprolol by means of
759 photo-oxidation processes, *Catalysis Today*, **2021**, 1-12,
760 <https://doi.org/10.1016/j.cattod.2021.06.014>

- 761 [27] Madhavan, J.; Grieser, F.; Ashokkumar, M. Combined advanced oxidation processes for the
762 synergistic degradation of ibuprofen in aqueous environments, *J. Hazard. Mater.* **2010**, 178, 202–
763 208, <https://doi.org/10.1016/j.jhazmat.2010.01.064>
- 764 [28] Eshaq, Gh.; Wang, Shaobin; Sund, Hongqi; Sillanpaa, Mika. Superior performance of
765 FeVO₄@CeO₂ uniform core-shell nanostructures in heterogeneous Fenton-sonophotocatalytic
766 degradation of 4-nitrophenol, *J. Hazard. Mater.* **2020**, 382, 121059-121059,
767 <https://doi.org/10.1016/j.jhazmat.2019.121059>
- 768 [29] Collins, T. J. TAML oxidant activators: A new approach to the activation of hydrogen
769 peroxide for environmentally significant problems, *Acc. Chem. Res.*, **2002**, 35, 782–90,
770 <https://doi.org/10.1021/ar010079s>
- 771 [30] Shah, V.; Verma, P.; Stopka, P.; Gabriel, J.; Baldrian, P.; Nerud, F.; Decolorization of dyes
772 with copper (II)/organic acid/hydrogen peroxide systems. *Appl. Catal., B*, **2003**, 46, 287–292,
773 [https://doi.org/10.1016/S0926-3373\(03\)00220-0](https://doi.org/10.1016/S0926-3373(03)00220-0)
- 774 [31] Bokare, A. D.; Choi, W.; Review of iron-free Fenton-like systems for activating H₂O₂ in
775 advanced oxidation processes, *J. Hazard. Mater.* **2014**, 275, 121-135,
776 <https://doi.org/10.1016/j.jhazmat.2014.04.054>
- 777 [32] Pettine, M.; Campanella, L.; Millero, F. Reduction of hexavalent chromium by H₂O₂ in
778 acidic solutions. *Environ. Sci. Technol.* **2002**, 63, 901–907, <https://doi.org/10.1021/es010086b>
- 779 [33] Codd, R.; Dillon, C. T.; Levina, A.; Lay, P. A. Studies on the genotoxicity of chromium:
780 from the test tube to the cell, *Coord. Chem. Rev.* **2001**, 216, (217), 537-582,
781 [https://doi.org/10.1016/S0010-8545\(00\)00408-2](https://doi.org/10.1016/S0010-8545(00)00408-2)
- 782 [34] Levina, A.; Lay, P. A.; Mechanistic studies of relevance to the biological activities of
783 chromium, *Coord. Chem. Rev.* **2005**, 249, 281-298.
- 784 [35] Anjum, M.; Kumar, R.; Barakat, M.A. Synthesis of Cr₂O₃/C₃N₄ composite for enhancement
785 of visible light photocatalysis and anaerobic digestion of wastewater sludge, *J. Environ. Manage.*
786 **2018**, 212, 65-76, <https://doi.org/10.1016/j.ccr.2004.02.017>
- 787 [36] Rajesh kumar, R.; Raj, Rishav; Venimadhav, A.; Weak ferromagnetism in band-gap
788 engineered α-(Fe₂O₃)₁-X(Cr₂O₃)_X nanoparticles, *J. Magn. Magn. Mater.* **2019**, 473, 119-124,
789 <https://doi.org/10.1016/j.jmmm.2018.10.007>
- 790 [37] He, X.; Antonelli, D. Recent advances in synthesis and applications of transition metal
791 containing mesoporous molecular sieves. *Angew. Chem. Int. Ed. Engl.*, **2002**, 214–229,
792 [https://doi.org/10.1002/1521-3773\(20020118\)41:2<214::AID-ANIE214>3.0.CO;2-D](https://doi.org/10.1002/1521-3773(20020118)41:2<214::AID-ANIE214>3.0.CO;2-D)

- 793 [38] Stănoiu, A.; Simion, C.E.; Diamandescu, L.; Tărăbășanu-Mihăilă, D.; Feder, M. NO₂ sensing
794 properties of Cr₂O₃ highlighted by work function investigations. *Thin Solid Films*, **2012**, 522,
795 395–400, <https://doi.org/10.1016/j.tsf.2012.09.003>
- 796 [39] Teixeira, V.; Sousa, E.; Costa, M. F.; Nunes, C.; Rosa, L.; Carvalho, M. J.; Collares-Pereira,
797 M.; Roman, E.; Gago, J. Spectrally selective composite coatings of Cr-Cr₂O₃ and Mo-Al₂O for
798 solar energy applications. *Thin Solid Films*, **2001**, 392, 320-326, [https://doi.org/10.1016/S0040-
799 6090\(01\)01051-3](https://doi.org/10.1016/S0040-6090(01)01051-3)
- 800 [40] Gunnewiek, R.F.K.; Mendes, C.F.; Kiminami, R.H.G.A. Synthesis of Cr₂O₃ nanoparticles
801 via thermal decomposition of polyacrylate/chromium complex, *Mater. Lett.* **2014**, 129, 54-56,
802 <https://doi.org/10.1016/j.matlet.2014.05.026>
- 803 [41] Peng, F.; Gao, H. Zhang, G; Zhu, Z.; Zhang, J.; Liu, Q. Synergistic Effects of Sm and C Co-
804 Doped Mixed Phase Crystalline TiO₂ for Visible Light Photocatalytic Activity Materials, **2017**,
805 10, 209-214, <https://doi.org/10.3390/ma10020209>
- 806 [42] Xiao, Q.; Si, Z.; Zhang, J.; Xiao, C.; Tan, X. Photoinduced hydroxyl radical and
807 photocatalytic activity of samarium-doped TiO₂ nanocrystalline. *J. Hazard. Mater.* **2008**, 150,
808 62–67, <https://doi.org/10.1016/j.jhazmat.2007.04.045>
- 809 [43] De la Cruza, D.; Arévalo, J.C.; Torres, G.; Bautista Margulis, R.G ; Ornelas, C.; Aguilar-
810 Elguézabal, A., TiO₂ doped with Sm³⁺ by sol-gel: Synthesis, characterization and photocatalytic
811 activity of diuron under solar light. *Catal. Today*, **2011**, 166, 152–158,
812 <https://doi.org/10.1016/j.cattod.2010.08.023>
- 813 [44] Sin, J.C.; Lam, S.M.; Lee, K.T. ; A.R. Mohamed, Photocatalytic performance of novel
814 samarium-doped spherical-like ZnO hierarchical nanostructures under visible light irradiation for
815 2,4- dichlorophenol degradation. *J. Colloid. Interface. Sci.*, **2013**, 401, 40–49,
816 <https://doi.org/10.1016/j.jcis.2013.03.043>
- 817 [45] Sukriti, P.; Chand, V.; Sing, Enhanced visible-light photocatalytic activity of samarium-
818 doped zinc oxide nanostructures, *J. Rare Earths*, **2020**, 38 (1), 29-38,
819 <https://doi.org/10.1016/j.jre.2019.02.009>
- 820 [46] Milne, W. I. ; Teo, K. B. K. ; Amaratunga, G. A. J.; Legagneux, P. ; Gangloff, L. ;
821 Schnell, J.-P., Semet, V.; Thien Binh, V.; Groening, O.; Carbon nanotubes as field emission
822 sources, *J Mater Chem.*, **2014**, 14, 933–943, <https://doi.org/10.1039/B314155C>
- 823 [47] Iijima, S.; Helical microtubules of graphitic carbon, *Nature* **1991**, 354. 56–58,
824 <https://www.nature.com/articles/354056a0>

- 825 [48] Jitianu, A.; Cacciaguerra, T.; Benoit, R.; Delpoux, S.; Béguin, F.; Bonnamy, S. Synthesis
826 and characterization of carbon nanotubes–TiO₂ nanocomposites, *Carbon*, **2004**, 42(5–6), 1147–
827 115, <https://doi.org/10.1016/j.carbon.2003.12.041>
- 828 [49] Lin, L.; Yu, D.; Wang, W.; Gao, P.; Bu, K.; Liu, B. Preparation of BiVO₄/Bi₂WO₆/multi-
829 walled carbon nanotube nanocomposites for enhancing photocatalytic performance, *Mater. Lett.*
830 **2016**, 185, 507–510, <https://doi.org/10.1016/j.matlet.2016.09.063>
- 831 [50] Abdullah, M. M.; Rajab, Fahd M.; Al-Abbas, Saleh M. Structural and optical
832 characterization of Cr₂O₃ nanostructures: Evaluation of its dielectric properties, *AIP Advances*
833 **2014**, 4, 027121- 027132, <https://aip.scitation.org/doi/10.1063/1.4867012>
- 834 [51] Franca, A.S.; Oliveira, L.S.; Ferreira, M.E.; Kinetics and equilibrium studies of methylene
835 blue adsorption by spent coffee grounds. *Desalination* **2009**, 249 (1), 267–272,
836 <https://doi.org/10.1016/j.desal.2008.11.017>
- 837 [52] Chamssedine, F.; Dubois, M.; Guérin, K.; Giraudet, J.; Masin, F.; Ivanov, DA.; Vidal, L.;
838 Yazami, R.; hamwi, A. Reactivity of carbon nanofibres with fluorine gas. *Chem. Mater.* **2007**,
839 19, 161–72, <https://doi.org/10.1021/cm061731m>
- 840 [53] Anandan, S.; Vinu, A.; Mori, T.; Gokulakrishnan, N.; Srinivasu, P.; Murugesan, V.; Ariga,
841 K.; Photocatalytic degradation of 2,4,6-trichlorophenol using lanthanum doped ZnO in aqueous
842 suspension, *Catal. Commun.* **2007**, 8, 1377–1382, <https://doi.org/10.1016/j.catcom.2006.12.001>
- 843 [54] El-Bahy, Z. M.; Ismail, A.A.; Mohamed, R. M. Enhancement of titania by doping rare earth
844 for photodegradation of organic dye (Direct Blue), *J. Hazard. Mater.* **2009**, 166, 138–143,
845 <https://doi.org/10.1016/j.jhazmat.2008.11.022>
- 846 [55] Singh, B. P.; Choudhary, V.; Teotia, S.; Gupta, T. K. ; Singh, V. N.; Dhakate, S. R.; Mathur,
847 R. B. Solvent Free, Efficient, Industrially Viable, Fast Dispersion Process Based Amine
848 Modified MWCNT Reinforced Epoxy Composites of Superior Mechanical Properties, *Adv.*
849 *Mater. Lett.* **2015**, 6 (2), 104–113, <https://www.vbripress.com/aml/articles/details/600>
- 850 [56] Anandan, K.; Rajendran, V. Studies on structural, morphological, magnetic and optical
851 properties of chromium sesquioxide (Cr₂O₃) nanoparticles: Synthesized via facile solvothermal
852 process by different solvents, *Materials Science in Semiconductor Processing* **2014**, 19(1), 136–
853 144, <https://doi.org/10.1016/j.mssp.2013.12.004>
- 854 [57] Taylor, D.W. *Optical Properties of Mixed Crystals*, 23, 1st Edition, (Chapter 2).North-
855 Holland, **1988**, 35–131.
- 856 [58] Faraz, M.; Naqvi, F.K.; Shakira, M.; Khare, N. Synthesis of samarium-doped zinc oxide
857 nanoparticles with improved photocatalytic performance and recyclability under visible light
858 irradiation, *New J. Chem.* **2018**, 42, 2295–2305, <https://doi.org/10.1039/C7NJ03927A>

- 859 [59] Pourfayaz, F.; Mortazavi, Y.; Khodadadi, A.; Jafari, S. H.; Boroun, S.; Naseh, M. V.; A
860 comparison of effects of plasma and acid functionalizations on structure and electrical property
861 of multi-wall carbon nanotubes, *Appl. Surf. Sci.* **2014**, 295, 66–70,
862 <https://doi.org/10.1016/j.apsusc.2014.01.005>
- 863 [60] Yu, T.; Shen, Z. X.; He, J.; Sun, W. X.; Tang, S. H.; Lin, J. Y. Phase control of chromium
864 oxide in selective microregions by laser annealing, *J. App. Phys.* **2003**, 93(7), 3951–3953,
865 <https://doi.org/10.1063/1.1558204>
- 866 [61] Mougina, J. ; Le Bihanb, T.; Lucazeauc, G. High-pressure study of Cr₂O₃ obtained by high-
867 temperature oxidation by X-ray diffraction and Raman spectroscopy, *J. Phys. Chem. Solids*
868 **2001**, 62, 553-563, [https://doi.org/10.1016/S0022-3697\(00\)00215-8](https://doi.org/10.1016/S0022-3697(00)00215-8)
- 869 [62] Larbi, T.; Ouni, B.; Gantassi, A.; Doll, K.; Amlouk, M.; Manoubi, T. Structural, Optical and
870 Vibrational Properties of Cr₂O₃ With Ferromagnetic and Antiferromagnetic Order: A Combined
871 Experimental and Density Functional Theory Study, *J. Magn. Magn. Mater.* **2017**, 444, 16-22,
872 <https://doi.org/10.1016/j.jmmm.2017.07.103>
- 873 [63] Rahman, A.; Mohamed, M.H.; Ahmed, M.; Aitani, A.M. Characterization of
874 chromia/alumina catalysts by X-ray photoelectron spectroscopy, proton induced X-ray emission
875 and thermogravimetric analysis, *Appl. Catal. A: Gen.* **1995**, 121, 2, 203-216,
876 [https://doi.org/10.1016/0926-860X\(94\)00204-5](https://doi.org/10.1016/0926-860X(94)00204-5)
- 877 [64] Lixi Wang; Jing Zhang; Qitu Zhang; Naicen Xu; Jie Song; XAFS and XPS studies on site
878 occupation of Sm^{3p} ions in Sm doped M-type BaFe₁₂O₁₉, *J.Magn. Magn. Mater.* **2015**, 377,
879 362–367, <https://doi.org/10.1016/j.jmmm.2014.10.097>
- 880 [65] Yan, X-B.; Tay, B. K.; Yang, Y. Dispersing and Functionalizing Multiwalled Carbon
881 Nanotubes in TiO₂ Sol, *J. Phys. Chem. B.* **2006**, 110, 25844-25849,
882 <https://doi.org/10.1021/jp065434g>
- 883 [66] Lin, Lu.; Dan, Yu.; Wang, Wei.; Gao, Pin.; Kaixuan Bu; Baojiang Liu; Preparation of
884 BiVO₄/Bi₂WO₆/multi-walled carbon nanotube nanocomposites for enhancing photocatalytic
885 performance, *Materials Letters*, **2016**, 185, 507-510, <https://doi.org/10.1016/j.matlet.2016.09.063>
- 886 [67] Zhou, Y.; Chen, C.H.; Wang, N.N.; Li, Y.Y. ; Ding, H.M. ; Stable Ti³⁺ self-doped anatase-
887 rutile mixed TiO₂ with enhanced visible light utilization and durability, *J. Phys.Chem.* **2016**,
888 C120, 6116–6124, <https://doi.org/10.1021/acs.jpcc.6b00655>
- 889 [68] Petrier, C.; Lamy, M.-F.; Francony, A.; Benahcene, A.; David, B.; Renaudin, V.;
890 Gondrexon, N. Sonochemical degradation of phenol in dilute aqueous solutions: comparison of
891 the reaction rates at 20 and 487 kHz, *J. Phys. Chem.* **1994**, 98, 10514–10520,
892 <https://doi.org/10.1021/j100092a021>

- 893 [69] Henglein, A. Chemical effects of continuous and pulsed ultrasound in aqueous solutions,
894 *Ultrasonics Sonochemistry* **1995**, 2, 115-121, [https://doi.org/10.1016/1350-4177\(95\)00022-X](https://doi.org/10.1016/1350-4177(95)00022-X)
- 895 [70] Tauber, A.; Mark, G. ; Schuchmann, H.P.; Sonntag, C. Sonolysis of tert-butyl alcohol in
896 aqueous solution, *J. Chem. Soc., Perkin Trans.* **1999**, 2, 1129-1136,
897 <https://doi.org/10.1039/A901085H>
- 898 [71] Slegers, C.; Baldacchino, G.; Le Parc, D.; Hickel, B.; Tilquin, B. Radical Mechanisms in the
899 Radiosterilization of Metoprolol Tartrate Solutions, *Pharmaceutical Research*, **2003**, 20, 12,
900 1977–1983, <http://www.ncbi.nlm.nih.gov/pubmed/14725362>
- 901 [72] Beltran, F.J. *Chemical Degradation Methods for Wastes and Pollutants: Environmental and*
902 *Industrial Applications*, 1st Ed., CRC Press, **2003**, 1-314
- 903 [73] Mehrdad, A.; Hashemzadeh, R. Ultrasonic degradation of Rhodamine B in the presence of
904 hydrogen peroxide and some metal oxide, *Ultrason. Sonochem.* **2010**, 17, 168–172,
905 <https://doi.org/10.1016/j.ultsonch.2009.07.003>
- 906 [74] Panda, D.; Manickam, S., Recent advancements in the sonophotocatalysis (SPC) and doped-
907 sonophotocatalysis (DSPC) for the treatment of recalcitrant hazardous organic water pollutants,
908 *Ultrason. Sonochem.* **2017**, 36, 481–496, <https://doi.org/10.1016/j.ultsonch.2016.12.022>
- 909 [75] Abbasi, M.; Asl, N.R. Sonochemical degradation of Basic Blue 41 dye assisted by Nano
910 TiO₂ and H₂O₂, *J. Hazard. Mater.* **2008**, 153, 942–947,
911 <https://doi.org/10.1016/j.jhazmat.2007.09.045>
- 912 [76] Tsou, T.-C. ; Yang, J.-L. Formation of reactive oxygen species and DNA strand breakage
913 during interaction of chromium (III) and hydrogen peroxide in vitro: Evidence for chromium
914 (III)-mediated Fenton-like reaction. *Chem.-Biol. Interact.* **1996**, 102, 133–153,
915 [https://doi.org/10.1016/S0009-2797\(96\)03740-4](https://doi.org/10.1016/S0009-2797(96)03740-4)
- 916 [77] Shi, X.; Dalal, N. S. ESR spin trapping detection of hydroxyl radicals in the reactions of
917 Cr(V) complexes with hydrogen peroxide. *Free Radical Res. Commun.* **1990**, 10, 17–26,
918 <https://doi.org/10.3109/10715769009145929>
- 919 [78] Shi, X.; Dalal, N. S.; Kasprzak, K. S. Generation of free radicals from hydrogen peroxide
920 and lipid hydroperoxides in the presence of Cr(III). *Arch. Biochem. Biophys.* **1993**, 302, 294–
921 299, <https://doi.org/10.1006/abbi.1993.1213>
- 922 [79] Bokare, A. D.; Choi, W. Advanced Oxidation Process Based on the Cr(III)/Cr(VI) Redox
923 Cycle, *Environ. Sci. Technol.* **2011**, 45, 9332–9338, <https://doi.org/10.1021/es2021704>
- 924 [80] Zhang, K.; Zhan, F.J.; Chen, M. L.; Oh, W. C. Comparison of catalytic activities for
925 photocatalytic and sonocatalytic degradation of methylene blue in present of anatase TiO₂-CNT

- 926 catalysts, Ultrason. Sonochem. **2011**, 18, 765–772,
927 <https://doi.org/10.1016/j.ultsonch.2010.11.008>
- 928 [81] Sin, J.-C.; Lam, S.-M.; Lee, K.-T.; Mohamed, A. Photocatalytic performance of novel
929 samarium-doped spherical-like ZnO hierarchical nanostructures under visible light irradiation for
930 2,4-dichlorophenol degradation, J. Colloid interface Sci. **2013**, 401, 40–49,
931 <https://doi.org/10.1016/j.jcis.2013.03.043>
- 932 [82] Zhao, D.; Wang, W.; Sun, Y.; Fan, Z.; Du, M.; Zhang, Q.; Ji, F.; Xu, X. One-step synthesis
933 of composite material MWCNT@BiVO₄ and its photocatalytic activity, RSC Adv. **2017**, 7
934 33671-33679, <https://doi.org/10.1039/C7RA04288D>
- 935 [83] Pham, V.L.; Kim, D.-G.; Ko, S.-O. Oxidative degradation of the antibiotic oxy tetracycline
936 by Cu@Fe₃O₄ core-shell nanoparticles. Sci. Total Environ. **2018**, 631–632, 608–618,
937 <https://doi.org/10.1016/j.scitotenv.2018.03.067>
- 938 [84] Malato, S.; Blanco, J.; Maldonado, M.; Fernández-Ibáñez, P.; Campos, A. Optimising solar
939 photocatalytic mineralisation of pesticides by adding inorganic oxidising species; application to
940 the recycling of pesticide containers, Appl. Catal. B: Environ. **2000**, 28, 3–4, 163-174,
941 [https://doi.org/10.1016/S0926-3373\(00\)00175-2](https://doi.org/10.1016/S0926-3373(00)00175-2)
- 942 [85] Kaur, S.; Singh, V. Visible light induced sonophotocatalytic degradation of Reactive Red
943 dye 198 using dye sensitized TiO₂, Ultrasonics Sonochemistry **2007**, 14, 531–537,
944 <https://doi.org/10.1016/j.ultsonch.2006.09.015>
- 945 [86] Anju, S.G.; Yesodharan, S.; Yesodharan, E.P. Zinc oxide mediated sonophotocatalytic
946 degradation of phenol in water, Chem. Eng. J., **2012**, 189–190, 84-93,
947 <https://doi.org/10.1016/j.cej.2012.02.032>
- 948 [87] Verma, A.; Kaur, H.; Dixit, D. Photocatalytic, sonolytic and sonophotocatalytic
949 degradation of 4-chloro-2-nitro phenol, Arch. Environ. Prot. **2013**, 39, 17-28,
950 <https://ur.booksc.eu/book/40422639/a1d1d6>
- 951 [88] Romero, V.; Marco, P.; Giménez, J.; Esplugas, S. Adsorption and Photocatalytic
952 Decomposition of the β -Blocker Metoprolol in Aqueous Titanium Dioxide Suspensions:
953 Kinetics, Intermediates, and Degradation Pathways, Int. J. Photoenergy, **2013**, 1-10,
954 <https://doi.org/10.1155/2013/138918>
- 955 [89] Ye, Y.; Feng, Y.; Bruning, H.; Yntema, D.; Rijnaarts, H.H.M. Photocatalytic degradation of
956 metoprolol by TiO₂ nanotube arrays and UVLED: Effects of catalyst properties, operational
957 parameters, commonly present water constituents, and photo-induced reactive species, Appl.
958 Catal. B: Environ. **2018**, 220, 171–181, <https://doi.org/10.1016/j.apcatb.2017.08.040>

- 959 [90] Benitez, F. J.; Acero, J. L.; Real, F. J.; Roldan, G.; Casas, F. Bromination of selected
960 pharmaceuticals in water matrices, *Chemosphere*, **2011**, 85, 9, 1430–1437,
961 <https://doi.org/10.1016/j.chemosphere.2011.08.022>
- 962 [91] Huerta Aguilar, C.A.; Pandiyan, T.; Arenas-Alatorre, J.A.; Narinder Singh, Oxidation of
963 phenols by TiO₂Fe₃O₄M (M = Ag or Au) hybrid composites under visible light, *Sep. Purif.*
964 *Technol.* **2015**, 265-278, <https://doi.org/10.1016/j.seppur.2015.05.019>
- 965 [92] Habibi, M. H.; Hassanzadeh, A.; Mahdavi, S. The effect of operational parameters on the
966 photocatalytic degradation of three textile azo dyes in aqueous TiO₂ suspensions, *J. Photochem.*
967 *Photobiol. A*, **2005**, 172, 1, 89-96, <https://doi.org/10.1016/j.jphotochem.2004.11.009>
- 968 [93] Wang, Y.; Yang, C.; Chen, A.; Pu, W. ; Gong, J. Influence of yolk-shell Au@TiO₂ structure
969 induced photocatalytic activity towards gaseous pollutant degradation under visible light, *Appl.*
970 *Catal. B: Environ.* **2019**, 251, 57–65, <https://doi.org/10.1016/j.apcatb.2019.03.056>
- 971 [94] Wang, K-H.; Hsieh, Y-H.; Chen, L-J. The heterogeneous photocatalytic degradation
972 intermediates and mineralization for the aqueous solution of cresols and nitrophenols, *J. Hazard.*
973 *Mater.* **1998**, 59, 251–260, [https://doi.org/10.1016/S0304-3894\(97\)00151-9](https://doi.org/10.1016/S0304-3894(97)00151-9)
- 974 [95] Pinedo, A.; López, E. M.; Zermeño, Leyva, B.; Serrano, B.; Moctezuma, E. Photocatalytic
975 Decomposition of Metoprolol and Its Intermediate Organic Reaction Products: Kinetics and
976 Degradation Pathway, *Int. J. Chem. React. Eng.* **2016**, 14(3), 809–820,
977 <https://doi.org/10.1515/ijcre-2015-0132>
- 978 [96] Moctezuma, E.; Leyva, E.; López, M.; Pinedo, A.; Zermeño, B.; Serrano, B. Photocatalytic
979 degradation of metoprolol tartrate. *Top. Catal.* **2013**, 56(18–20), 1875–1882,
980 <https://link.springer.com/article/10.1007/s11244-013-0119-x>
- 981 [97] Leyva, E.; Moctezuma, E.; López, M.; Baines, K. M. ; Zermeño, B. Photocatalytic
982 degradation of β -blockers in TiO₂ with metoprolol as model compound, Intermediates and total
983 reaction mechanism, *Catal. Today*, **2019**, 323, 14-25,
984 <https://doi.org/10.1016/j.cattod.2018.08.007>
- 985 [98] Abramović, B.; Kler, S.; Šojić, D.; Laušević, M.; Radović, T.; Vionec, D. Photocatalytic
986 degradation of metoprolol tartrate in suspensions of two TiO₂-based photocatalysts with different
987 surface area. Identification of intermediates and proposal of degradation pathways, *J. Hazard.*
988 *Mater.* **2011**, 198, 123-132, <https://doi.org/10.1016/j.jhazmat.2011.10.017>
- 989 [99] Song, W.; Cooper, W.J. ; Mezyk, S.P. ; Greaves, J. ; Peak, B.M. Free Radical Destruction of
990 β -Blockers in Aqueous Solution, *Environ. Sci. Technol.* **2008**, 42, 1256-1261,
991 <https://doi.org/10.1021/es702245n>